UNIFIED CONSTITUTIVE MATERIALS MODEL DEVELOPMENT AND EVALUATION FOR HIGH-TEMPERATURE STRUCTURAL ANALYSIS APPLICATIONS

Robert L. Thompson, NASA Lewis Research Center
Michael T. Tong, Sverdrup Technology, Inc.
Cleveland, Ohio, USA

Abstract

Unified constitutive material models were developed for structural analyses of aircraft gas turbine engine hot section components with particular application to an isotropic material used for combustor liners. Differential forms of models independently developed were considered in this study. These models combine the interactions of time-dependent (creep) and time-independent (plasticity) inelastic behavior of a material. Predicted stress-strain responses from these models were evaluated against cyclic isothermal and nonisothermal test results for uniaxial specimens of a nickel-base superalloy. The unified models were implemented in a nonlinear structural analysis code. Two unique NASA Lewis test facilities were used in the evaluation of the models for complex geometry specimens and evaluation of advanced temperature and hightemperature strain measurement instrumentation. Predicted nonlinear structural responses from one of the models for a flat plate and a segment of a conventional combustor liner are presented.

Introduction

This paper discusses: (1) the development, evaluation and validation of unified (viscoplastic) constitutive material models with application from simple (cylindrical bar) to complex (engine component) geometry specimens, (2) the implementation of the unified models into a nonlinear finite element structural analysis code, and (3) the application of the analytical tools for heat transfer and structural analyses of gas turbine engine hot section components. The use of unified models in nonlinear structural analysis codes is a radical departure from the classical (plasticity based) nonlinear structural analysis approach. The basis for this radical departure hinges on results from previous analytical studies of gas turbine engine hot section components such as turbine blades[1] and combustor liners[2].
These studies showed that nonlinear structural analysis results based on classical methods did not accurately predict the structural response of the hot section components.

Today's gas turbine engine hot section components operate in severe thermomechanical environments. The complex cyclic thermomechanical loading histories and high temperatures imposed on the hot section components result in inelastic material deformation and low-cycle thermal fatigue. Unified (viscoplastic) models are better able to characterize the inelastic material behavior than the classical plasticity based methods. The unified models account for the interactions between time-independent (plasticity) and time-dependent (creep/stress relaxation).

Thus they avoid the summation of inelastic strain into separate plastic and creep components or the specifying of yield surfaces as required by the classical theories.

Recent results of the NASA Lewis in-house efforts on the development and evaluation of nonlinear constitutive relations for high temperature applications are reported. The in-house efforts represent a substantial part of the High Temperature Structural Mechanics program at Lewis, but it is much broader in scope and involves industry, academia, and other government agencies. Much of this research, both in-house and out-of-house, has been funded by the Hot Section Technology (HOST) project at NASA Lewis.

Constitutive Models

Four unified constitutive models were evaluated in this study. The criteria used for the evaluation were: (1) ability to accurately characterize the cyclic isothermal as well as nonisothermal (in-phase and out-of-phase) inelastic behavior of an isotropic nickel base superalloy, Hastelloy-X, (2) applicability over the temperature and temperature rate as well as strain and strain rate ranges of interest for typical gas turbine engine mission cycles for hot section components, (3) extendability to accurately predict multiaxial states of stress and strain of hot section components under complex thermomechanical loading conditions, and (4) integratability of or ease of implementation of models in nonlinear finite element structural analysis computer codes.

A brief description of each of the four models, the Miller, the Bodner, the Krieg, Swearengen, and Rhode (KSR), and the Walker models based on their uniaxial differential forms is presented. The models incorporate coupled time-independent (plasticity) and time-dependent (creep) material behavior. The multiaxial forms of the models along with more detailed discussions and results are found in the references cited.

Three of the four viscoplastic models can be described by a set of constitutive equations that have the following basic form:

$$\dot{\epsilon}_I = f \left[\frac{S - \Omega}{K} \right] \tag{1}$$

$$\dot{\Omega} = h_1(\Omega, K) \, \dot{\epsilon}_I - d_1(\Omega, K) \, \Omega \, |\dot{\epsilon}_I| - r_1(\Omega, K) \tag{2}$$

$$\dot{K} = h_2(\Omega, K) \, |\dot{\epsilon}_I| - d_2(\Omega, K) \, K \, |\dot{\epsilon}_I| - r_2(\Omega, K) \tag{3}$$

Equation (1) is the flow law where the inelastic strain rate vector, $\dot{\epsilon}_I$, is related to the deviatoric stresses, $\underline{s}$, and two internal state variables, $\underline{\Omega}$ and K. The tensorial internal state variable, commonly called the equilibrium or back stress, Ω, defines the kinematic or directional hardening while the scalar internal state variable, commonly called the drag stress, k, defines the isotropic hardening (softening). Equations (2) and (3) are evolutional equations which describe the growth laws of the internal state variables. Both hardening and recovery terms are included in these equations. In these equations, h_1 and h_2 are functions describing hardening, d_1 and d_2 are functions describing dynamic recovery, and r_1 and r_2 are functions describing static thermal recovery. As shown, these functional forms are generally functions of the internal state variables but they can be constants for some materials. Temperature effects on the inelastic strain rate are generally accounted for by having some of the material constants vary with temperature. They are also accounted for by the addition of temperature rate terms in the growth laws of some of the models.

Walker Model

The flow law and growth laws in their differential uniaxial forms for the Walker model[3,4] are

$$\dot{\epsilon}_I = \left[\frac{\sigma - \Omega}{K} \right]^n \text{sign}(\sigma - \Omega) \qquad (4)$$

$$\dot{\Omega} = (n_1 + n_2)\,\dot{\epsilon}_I - (\Omega - \Omega_0 - n_1\epsilon_I) \left\{ [n_3 + n_4 \exp(-n_5|\epsilon_I|)]|\dot{\epsilon}_I| + n_6|\Omega|^{m-1} \right\} \qquad (5)$$

$$\dot{K} = n_7 K_2 \exp(-n_3|\epsilon_I|)|\dot{\epsilon}_I| \qquad (6)$$

A power law is employed in the inelastic strain rate equation, equation (4). The hardening term in the back stress evolutional equation, equation (5), varies linearly with inelastic strain rate. The recovery term in equation (5) contains both static and thermal recovery terms, while no recovery term is provided for in equation (6). The strain hardening term in the drag stress evolutional equation, equation (6), is nonlinear and dependent on cumulative inelastic strain.

The thirteen material constants, $n_1 > n_8$, Ω_0, n, m, k_1 and k_2 are assumed to be temperature dependent. K_1 is the initial value for drag stress and Ω_0 indicates the amount by which the stress-strain curve is shifted along the stress axis to produce the difference in tensile and compressive behavior (Bauschinger effect). With no isotropic material hardening, material constants K_2 and n_7 are zero so that the drag stress remains constant. The determination of material constants requires cyclic tests at various strain rates, stress relaxation tests, and monotonic tensile tests.

Miller Model

The Miller model [3,5] is based on both metallurgical and experimental observations. For this model, the flow and growth laws in their uniaxial differential forms are

$$\dot{\epsilon}_I = B\Theta^* \left\{ \text{Sinh} \left[\frac{\sigma - \Omega}{K} \right]^{1.5} \right\}^n \text{sign}(\sigma - \Omega) \qquad (7)$$

$$\dot{\Omega} = H_1\dot{\epsilon}_I - H_1 B\Theta^* \left[\text{Sinh}(A_1|\Omega|) \right]^n \text{sign}(\Omega) \qquad (8)$$

$$\dot{K} = H_2|\dot{\epsilon}_I| \left[C_1 + |\Omega| - (A_2/A_1)K^3 \right] - H_2 C_2 B\Theta^* \left[\text{Sinh}(A_2 K^3) \right]^n \qquad (9)$$

where

$$\Theta^* = \exp\left\{ \left[\frac{-Q}{0.6kT_m} \right] \left[\ln(0.6T_m/T) + 1 \right] \right\} \qquad (10)$$

for
$$T < 0.6\ T_m$$
and

$$\Theta^* = \exp(-Q/kT) \qquad (11)$$

for
$$T \geq 0.6\ T_m$$

A hyperbolic sine function is employed in the inelastic strain rate equation, equation (7). The growth rate of the back stress varies linearly with inelastic strain rate in equation (8) while a hyperbolic sine function dependence is assumed in the static thermal recovery term. Note that a dynamic recovery function is not provided for in equation (9). Typically, under monotonic loading with constant strain rate, the back stress resulting from equation (8) exhibits trilinear behavior. Cyclic hardening or softening is introduced through the drag stress and results from the initial value of drag stress.

Temperature dependence is introduced through the variable Θ^*, an Arrhenius function, as defined in equations (10) and (11). T_m is the melting temperature of the material. The inclusion of Θ^* in the recovery functions of the evolutional equations (8) and (9) simulates thermal recovery. Moreover, since the initial value of the drag stress is a function of temperature, it has to be determined for the temperature of interest.

The nine material constants, n, A_1, A_2, B, C_1, C_2, H_1, H_2 and Q are independent of temperature. N, A_1, B, and Q are determined from steady-state creep tests while C_1, C_2 and H_1 are determined from cyclic stress versus strain data. The starting value for k depends on the initial strength of the material in tension and compression. The initial value of K is determined from the experimental yield strength, temperature and strain rate. H_2 provides for control of the isotropic hardening.

Krieg, Swearengen and Rhode Model (KSR)

The KSR model[3,6] is based on the current microstructure of the material. The constitutive equations in their uniaxial differential forms are:

$$\dot{\epsilon}_I = C_o \left[\frac{\sigma - \Omega}{K} \right]^n \text{sign} \, (\sigma - \Omega) \qquad (12)$$

$$\dot{\Omega} = C_1 \dot{\epsilon}_I - C_2 \Omega^2 \left[\exp(C_3 \, \Omega^2) - 1 \right] \text{sign}(\Omega) \qquad (13)$$

$$\dot{K} = C_4 |\dot{\epsilon}_I| - C_5 (K - K_o)^m \qquad (14)$$

A power law similar to that in Walker's model is employed in the inelastic strain rate equation, equation (12). The power law models steady-state creep when both the back and drag stresses reach a saturated state. The recovery term in equation (13) describes the temperature-dependent changes in the dislocation network whereas in equation (14) it describes the effect of dislocation pile-ups. The hardening functions in equations (13) and (14) are assumed to be constants, that is, C_1 and C_4 are constants. As was the case in Miller's model, since C_1 is constant and the recovery function is an exponential, the back stress takes on a trilinear character.

The KSR model is formulated around an isothermal condition. Thus all the material constants must be determined at a constant temperature, as is the case for Walker's model. The nine material constants, C_0, N, $C_1 \rightarrow C_5$, K_0 and m are determined from steady-state creep tests, primary creep tests, and stress drop tests. K_0 is the drag stress at the annealed state.

Bodner Model

The exception to the basic equations (1) to (3) is the Bodner model.[7,8] The flow law for this model is

$$\dot{\epsilon}_I = D \exp\left[-0.5(Z^3/3J_2)^n\right] \frac{S}{\sqrt{J_2}} \qquad (15)$$

where D and n are material constants, J_2 is the second invariant, and Z is the scalar internal state variable.

There are two major differences between equations (15) and (1). First, the Bodner model assumes the inelastic strain rate vector to be coincident with the direction of the deviatoric stress vector, S, whereas the back stress models assume it to be coincident with the direction of $S - \omega$. Second, the Bodner model uses the plastic work rate, w_p, as the measure of the hardening rather than the inelastic strain rate.

In the Bodner model, isotropic and kinematic hardening are modelled by partitioning the internal state variable into two components, Z_I and Z_D, or in rate form

$$\dot{Z} = \dot{Z}_I + \dot{Z}_D \qquad (16)$$

The evolutional equations for the internal rate components are

$$\dot{Z}_I = h_1 (Z_1 - Z_I) \dot{W}_p - r_1 \qquad (17)$$

$$\dot{Z}_D = h_2 (Z_D) - d(Z_D) \dot{W}_p - r_2 \qquad (18)$$

Z_1 is a constant in equation (17) and is the saturated value of Z_I. Cyclic hardening or softening is controlled by Z_I and depends on whether the initial value of Z_I is less than or greater than Z_I.

There are nine material constants to be determined for the Bodner model. Generally, for most isotropic materials, three of the material constants are found to be temperature-dependent. Most of the material constants are determined from uniaxial monotonic tensile and creep tests.

Evaluation of Unified Constitutive Models

Predictions from the four unified (visco-plastic) models described previously are compared with experimental data generated in the NASA Lewis Structures and Fatigue Laboratory. Both cyclic isothermal and nonisothermal data were generated with uniaxial Hastelloy-X specimens for the comparisons and evaluations of the models. None of these tests was used to determine the material constants for the models.

Experimental Apparatus

The loading frame used in the experiments was designed and built at NASA Lewis. It is rated for loads of ±9072 kg (±20,000 lb) and uses a die set to maintain rig alignment during specimen loading. An MTS 442 controller was used as the servocontroller for the rig. The specimen was attached to the loading frame with a split grip which can accommodate button-head and threaded specimen ends. Cooling of the upper and lower grips was achieved by wrapping 9.5 mm (3/8 in.) copper tubing around the grips and running recirculating water through the turbine.

The calibration of the load cell and fine tuning of the load conditioner were accomplished by using a special calibration specimen and a SR-4 strain indicator. The calibration specimen has a square cross-section with strain gages mounted on each of the four faces. Semianually, both the calibration specimen and the SR-4 strain indicator are checked and adjusted for accuracy by the National Bureau of Standards (N.B.S.).

Longitudinal strains were measured by an MTS high temperature axial extensometer with a 25.4 mm (1 in.) gage length. For protection against the high test temperatures, the extensometer is water cooled and is equipped with a watercooled heat shield. Longitudinal displacements were sensed by pointed quartz probes. To assure that the probes did not slip, dimples were made on the specimen and the probe points were placed in these dimples.

Calibration of the extensometer was carried out on a biaxial calibration fixture. Longitudinal displacements can be measured up to 1.27 x 10^3 mm (50 millionths of an inch (0.000050 in.)) with the calibration fixture. The range card for the strain conditioner was set up so that ±10 V = ±10 mil (0.010). The calibration was checked after every other test.

The tests were performed in strain control over a longitudinal strain range of ±0.3 percent at a constant strain rate of 10^{-3}/s. To control the tests in strain control, a Wavetek waveform generator (Model 175) was used. The wave shape programmed into the generator was a triangular wave with an electrical signal of ±3 V. The electrical signal is the commend input signal that the servosystem is made to follow.

Elevated specimen temperatures were achieved by high frequency induction heating. The induction unit used as a Lepel 5.0 kW high frequency generator with a Research Institute Panel Packer (Model 61011) for a temperature controller. High temperatures were sensed with the use of Chromel-Alumel thermocouples which were spot-welded to the specimen. One thermocouple was used as a feedback control for the Panel Packer and other one was used to monitor the temperature with the aid of a Doric Trendicator.

An extensive thermal gradient study was conducted to assure that the temperature distribution over the specimen gage length was within ±5°C (±10°F) of the nominal test temperature. This study concentrated mainly on the coil design for the induction heating. It was decided that the only two design limitations of the coil would be: (1) the coil's diameter was large enough to allow the specimen to slip through it; (2) the coil must have adequate openings between the "turns" of the coil that would allow the extensometer probes to have "unrestrictive movement." With the aid of a specially thermocoupled specimen, several coil configurations were tried. The design giving best results was a seven turned coil of 3.18 mm (1/8 in.) flattened cooper tubing. The coil turns spacing was such that there were three turns above the upper probe of the extensometer, one turn in between the upper and lower probes, and three turns below the lower probe. The temperature gradient was checked for all test temperatures, and was frequently verified during the testing program.

Measurements of load and strain were taken with the aid of a strip chart recorder and an X-Y recorder. The X-Y recorder was used for recording load versus strain (hysteresis loops). The strip chart recorder was used to obtain stress range and number of cycles for strain hardening curves. For further information on specimens, grips, loading frame, strain measurements, temperature measurements, and other laboratory conditions, see[9].

Uniaxial Isothermal Comparisons

Shown in figures 1, 2, 3, and 4 are predicted uniaxial isothermal hysteretic plots (axial stress versus total axial strain) from the four unified models at four temperatures. The four temperatures are 427°C (800°F), 593°C (1100°F), 760°C (1400°F), and 982°C (1800°F). Experimental data are plotted for two of these temperatures. The strain rate is 0.0001 in/in-sec and the strain range is ±0.3 percent. The test data and predictions were compared after three thermal cycles.

The temperature range selected is typical of in-service combustor liners. The strain range and rate selected, however, are only representative of in-service combustor liners, since liners undergo complex cyclic multiaxial changes in strain.

The experimental data show that the Hastelloy-X material is stronger in tension than in compression. The four models do not, in general, characterize this behavior accurately. The Walker model predicts hysteresis loops that are too shallow at the knees, particularly at the lower temperatures. The KSR model predicts hysteresis loops that flatten out at their tops and bottoms, much too quickly, indicating the back stress rate goes to zero quickly. It also underpredicts both the peak tensile and compressive stresses. The Miller model produces hysteresis loops at the intermediate temperatures that are trilinear in shape, as pointed out earlier. It overpredicts the peak tensile and compressive stresses, and at 472°C (800°F), it predicts an elastic response. The predictions using the Bodner model more closely match the experimental data than the other models at the low and intermediate temperatures. However, at the highest temperature 982°C (1800°F), the Bodner model predictions do not agree with the other three models. Qualitatively, these models are capable of characterizing in an overall sense the inelastic material behavior. But quantitatively, the models need further refinements to accurately characterize the shapes and levels of the uniaxial isothermal hysteresis loops for the limited set of isothermal test conditions considered here.

Other considerations of how well a model performs are its numerical stability and CPU time [10]. This is illustrated by comparing the computer times for the four models for the integration of a hysteresis loop. The computer integration times for the hysteresis loops shown in figure 1 for the four models are 73 cpu seconds (Walker); 44 cpu seconds (KSR); 52 cpu seconds (Bodner); and 33 cpu seconds (Miller). The time differences result primarily from the different functional forms assumed for the flow law. The explicit Euler forward integration scheme was used for the four models.

There are other concerns about the models such as whether or not a nonisothermal constitutive model can be based on isothermal test data. According to Ref.[11], it was shown that the information contained in isothermal cyclic hardening data is not sufficient to predict hardening behavior under complex cyclic thermomechanical conditions. Other model concerns are the validity of multiaxiality proportional and nonproportional predictions based on uniaxial test data. Many of these concerns have yet to be addressed.

Uniaxial Nonisothermal Comparisons

As stated earlier, one of the concerns about these models, which for the most part are based on isothermal test data, is their ability to accurately predict stresses and strains for cyclic thermomechanical conditions. To begin to assess this effect both in-phase and out-of-phase (temperature and strain) uniaxial nonisothermal tests were conducted at NASA Lewis. Comparisons of experiment and predictions are presented for two thermomechanical deformation (TMD) tests.

Shown in Figure 5 is a comparison of in-phase uniaxial nonisothermal (TMD) experimental data with predictions from the four unified models. The strain and temperature variations are linear (saw tooth) and in-phase. The strain rate is 0.000046 in/in-sec, the total strain range is ±0.3 percent, and the temperature range is 395° to 606°C (743° to 1123°F). The period is 295.3 sec/cycle. The temperature range selected is representative of a location on a combustor liner near the cooling holes, one of the several critical failure locations on a combustor liner. The experimental data show the in-phase hysteresis loop to be nearlyelastic. Three of the four constitutive models, namely Bodner, Miller and KSR, predict fairly well this linear response. The Walker model, however, predicts more inelastic response than the others and the hysteresis loop is displaced upward. Here again, qualitatively, the models do a reasonable job at predicting the cyclic stress-strain response compared to the experimental data but quantitatively, to accurately predict the shape and levels of the cyclic response requires further refinements to the models. Tests at other conditions, for example, temperatures up to 1000°C, are continuing and additional comparisons between experiment and predictions are underway.

Shown in Figure 6 is a comparison of out-of-phase uniaxial nonisothermal (TMD) experimental data with predictions from the four unified models. The strain and temperature variations are linear and 180 degrees out of phase. The other test conditions are identical to those of the in-phase tests.

Of the four models, the Bodner model more closely matches the experimental data. The Walker model is the next best but the knees of the hysteresis loop are too shallow and the stress levels are slightly below the experimental data. The Miller model predicts a hysteresis loop with a very narrow inelastic strain range and peak tensile and compressive stresses much greater than the experimental data. The KSR model predicts a hysteresis loop that shows the effect of numerical stability difficulties. Qualitatively, the Walker and Bodner models do a fair job at predicting the uniaxial out-of-phase nonisothermal hysteresis response compared to the experimental data, but quantitatively, to accurately predict the shape and levels of the cyclic response, further refinements to the models are required. Additional tests are underway to expand the data base so that additional comparisons can be made.

Bench-Top Flat Plate Test Facility

Flat plate specimens are radiantly heated in the Bench-Top rig (shown in Fig. 7) to induce thermal stresses and strains in the specimens. Quartz lamps are used to cyclically heat the specimens to temperatures and temperature gradients similar to those experienced by in-service gas turbine engine combustor liners. A typical engine mission cycle (take-off, cruise, landing and taxi conditions) of three-to-four hours duration is simulated in two-to-three minutes on the rig. This cycle time is felt to be adequate to capture the time-independent and the time-dependent (creep/plasticity) interactions that result in inelastic deformation as well as the low-cycle thermal fatigue phenomena of in-service liners.

The Bench-Top rig has two primary purposes. The first is to generate a large quality thermal cyclic (TMD) data base for a flat plate specimen, a simple structural test. Flat plate specimens are more analyzable from both a thermal and structural viewpoint than complex geometry hot section components such as combustor liners. The second is to use the rig as a test bed to evaluate advanced instrumentation that has potential use on the Structural Component Response rig, which is described in a later section. The data base is used to evaluate the newly developed analytical tools. The rig also offers flexibility in that it provides for a variety of test conditions to be easily run. For example, a test run can be started and stopped several times during a test and the plate inspected and/or test conditions changed.

Description of Bench-Top Rig

The quartz lamp heating system consists of four quartz lamps. The lamps are rated at 6,000 watts, 480 volts. Total rated power is 24 kW. The 305 mm (12-in) long lamps are located about 63.5 mm (2-1/2 inches) below the test specimen, and a frosted quartz window separates the lamps from the specimen.

Power provided to the test stand is three-phase, 480 volts. A Silicone Control Rectifier (SCR), one of the four which controls the Structural Component Response rig distributes the power to the lamps.

A Dual Loop Programmable Controller controls the power signal to the SCR. The controller can be used in any of four control modes, namely: set point, deviation, process variable, and proportional. The remote set point control mode is used for most of the tests to impose a desired temperature history at a point on the hot surface of a plate. The power history programmed into the controller is obtained from a set of parametric power versus temperature plots. The controller can be automatically set to control the number of thermal cycles for each test.

Cooling air to the rig is provided by service air. The lamps are air cooled. Air flow of up to 0.045 kg/sec (0.1 lb/sec) is available to cool one side of a flat plate specimen. The cooling air to the specimen can be preheated with precise control up to 400°F (204°C) by a vitiated heater. The cooling air to the plate is introduced to the plate through a manifold. All inlet and outlet flow conditions are sensed and monitored, and are available as visual readouts in the control room or can be stored on the Lewis IBM 370 computer using the ESCORT II Data Acquisition system.

Cooling water is required to cool the test section. A total of six separate cooling lines are used for this purpose in an open loop system. Here again, all inlet and outlet flow conditions are sensed and monitored, and are available as visual readouts or can be stored on the IBM 370 computer.

A complex system of safety interlocks is provided to assure safe operation of the rig, to protect the personnel, and to avoid damage to the test facility, rig, and specimen. The system includes alarms and lights as well as automated and manual override emergency shutdown controls when test condition limits, low or high depending on the condition, have been exceeded or violated.

Also, alarms are part of the computer data acquisition system for both the facilities and research data.

Description of Test Plate and Data Acquisition

A photograph of an instrumented flat plate test specimen is shown in figure 8. The Hastelloy-X specimen has dimensions of 203 x 127 x 1.27 mm (8 x 5 x 0.05 in.). A total of ten Chromel/Alumel ball type thermocouples were used to obtain hot and cool surface temperatures of the flat plate specimen. Seven thermocouples were mounted on the cool side and three on the hot side of the plate. An Infrared (IR) Thermovision system, manufactured by Inframetrics, Inc., Bedford, Massachusetts, was also used to obtain temperature data. IR data were obtained on the cool surface of the plate. The cylindrical quartz viewport located at the top of the test section (see Fig. 7) provided for easy visual access for the IR camera.

Both the thermocouple and IR temperature data were recorded. The ESCORT II Data Acquisition system, developed at Lewis, was used to store the thermocouple data on the IBM 370 computer and/or on hard copy devices located in the control room as the tests were being conducted. Additional software including graphics was developed for easy access and plotting of the stored data. The raw IR temperature data were recorded on a Video Cassette Recorder (VCR). A computer system with an Apple IIe at its center is coupled with the IR system. With this system the IR VCR data can be reviewed and analyzed in real time. Software was also developed for later IR data reduction and analysis.

Experimental Results

A series of parametric tests was conducted to determine the power settings needed to ensure that a desired temperature history could be imposed on the test plate at a point. The point monitored was a hot side thermocouple. Figure 9 shows the maximum steady-state temperature of the Hastelloy-X plate plotted against various applied power settings for three cooling airflow rates (all at ambient temperature) to the plate. The solid points show the effect of preheating the cooling air to 221°C (430°F). A 60-percent power setting with no cooling air to the specimen results in a maximum temperature on the hot side of the plate of about 982°C (1800°F), while convectively cooling the plate reduces the maximum temperature of the specimen appreciably. Note that preheating the cooling air increases the plate temperature at the lower power settings but has little effect on plate temperature at the higher power settings. The capability to vary cooling air temperature and flow rate as well as the power to control plate temperature resulted in a flexible test system.

Figure 10 shows the cool-side steady-state plate temperatures for three power settings for an intermediate cooling air flow of 0.227 kg/sec (0.5 lb/sec). The cooling air was preheated to 221°C (430°F). The seven cool-side and three hot-side thermocouple locations are shown in the sketch. Both horizontal (axial) and vertical (transverse) centerline plate temperatures are plotted as functions of the thermocouple locations. The plate temperatures are nonuniform because of the lamp configuration and cooling air flow patterns on the plate. The intermediate cooling flow and 90 percent power resulted in axial temperatures comparable to those of in-service conventional combustor liners. The transverse temperatures are representative of the circumferential temperatures of in-service combustor liners between the fuel nozzles. Temperatures of a combustor liner can be simulated on the flat plate rig but the dimensions are different and the curvature effects cannot be accounted for.

Hot-side temperatures were also measured. Hot-side temperatures in this case are about 17°C (30°F) hotter than the cool-side temperatures plotted in figure 10. IR data of the cool side were also obtained, but a discussion of the IR data is deferred and is presented in the Annular rig results section.

The parametric data were used to determine power settings for thermal cycle (TMD) tests. Results from one of the TMD tests of a flat plate are shown in figures 11 and 12. Figure 11 shows the power history, which consisted of a ramp up from 5 to 100 percent in 6 seconds, a hold of 80 seconds, a ramp down from 100 to 5 percent in 6 seconds, a hold of 50 seconds. The 142 second total cycle time simulated take-off, cruise, landing and taxi conditions of an actual engine mission cycle. Cooling airflow to the plate was 0.045 kb/sec (0.1 lb/sec) and the preheater was used to preheat the cooling air to 221°C (430°F). Figure 12 shows the maximum plate temperature as a function of time. It varies from about 900°C (1650°F) at the maximum power level to 260°C (500°F) at the minimum power level. About 35 seconds was required for the plate to reach stable temperature conditions for both the heat-up and cool-down phases. Figure 13 shows that the thermal cycling of a test plate produces temperatures that are stable and reproducible at the minimum and maximum power levels.

The measured plate temperatures are not only used as thermal loads (input) to the structural analysis computer programs, but also as boundary conditions and for determination of heat transfer coefficients. Heat transfer analyses are performed to determine plate temperatures at other locations. The predicted temperatures were used as thermal loads to the structural analysis programs.

High-Temperature Strain Measurement

Improvements to and validation of constitutive and low-cycle fatigue life models for improved design of hot section components have been severely hampered due to an inability to measure large nonisothermal strains at elevated temperatures, that is, above 538°C (1000°F). A small (1 mm to 3 mm length) wire resistive wire strain gage is most commonly used to measure local strain. These gages, however, suffer from extreme variations or anomalous behavior of electrical resistance at elevated temperature and are also limited to a range of a few thousand microstrain. They have yet to be successfully used for the measurement of static strains experienced by hot section components. Technology in this area, however, is advancing and new strain gage materials are being proposed. Tests of these advanced gages as well as noncontact devices such as proximity transducers and laser interferometry are and will be conducted on the Bench-Top rig.

1505f

Preliminary results of using one such noncontact device, a Laser Specklegram system, to measure strain are presented here.

The objective of the research program, a cooperative effort with the United Technologies Research Center (UTRC), a division of United Technologies, East Hartford, Connecticut, was to perform a demonstration test of laser speckle photography by measuring strain of a flat plate specimen. The potential for the use of a laser system to measure strain was established in laboratory tests described in reference[12].

The equipment for the Laser Specklegram system was mounted on an optics pallet at UTRC and delivered to NASA Lewis for testing. The tele-centric lens and automatic plate changer were mounted together with the solenoid for operating the lens shutter. High energy mirrors and a diverging lens were used to direct the illumination beam onto the surface of the flat plate, through the viewport. The pulsed laser was mounted on adaptor plates designed to hold it at the proper height. Figure 7 shows a picture of the optics pallet, test rig, and IR camera.

Photographs, commonly called specklegrams, of the test plate lit by laser light, are used to measure plate displacement. The image speckles, which result from diffuse reflection of coherent light, move as if attached to the plate surface when that surface is in focus, and they form a high contrast image pattern which uniquely defines each region of the plate surface. Specklegrams are commonly recorded as double exposures, that is before and after a plate displacement.

Evaluation of a double-exposure specklegram is commonly done by passing a narrow, converging beam of light through a small region of the specklegram and observing the optical Fourier Transform displayed where the beam comes to focus. Lateral displacements between the speckle patterns resulting from the two exposures generate fringes in the transform plane that uniquely define the speckle displacement. The difference between speckle displacements at neighboring regions can generally be related to strain. An Automated Interferometric Photocomparator system is used to provide automatic readout of strain distributions from the speckle photographs.

The double-exposure specklegram technique has limitations however. First, the displacement range is limited by the need to measure fringes in the transform plane. The displacement must be large enough to generate at least one or two fringes but cannot be so large as to generate more than about 25. Thus strain measurement can be hampered by large bulk displacements that accompany the plate deformation. Second, the accuracy with which hole fringe spacing and orientation may be measured is limited to one or two percent. This requires specklegrams to be recorded with low f/number lenses in order to obtain high resolution of plate displacements. On the other hand, such lenses reduce depth of focus and cause errors due to defocusing.

Shown in figure 14 are representative strain measurements on a test plate obtained from the Laser Specklegram system. Strain measurements are plotted as principal strain vectors for a 50.8 cm (2 in.) diameter circle on the plate. These measurements were taken before and after the test specimen was thermally cycled. In other words, this is a measure of the permanent distortion of the plate. During the test, the flat plate specimen underwent free thermal expansion. The plate was thermally cycled from 149°C (300°F) to 899°C (1650°F) and back to 149°C (300°F). The temperature increments for the thermal cycle were about 93°C (200°F) with hold times during each increment of approximately 2 minutes. Speckle-grams were taken for each increment. However, because of the nonuniform heating of the plate, as was noted previously, thermal strains and stresses were introduced in the plate. This eventually resulted in a warping or buckling of the plate. Figure 8 shows this warpage.

Although good correlations were obtained for a thermal cycle, the photocomparator analysis of the double-exposure specklegrams for each temperature increment showed poor or no correlation. The major difficulty of this technique was attributed to the movement of the test plate. It is believed that the in and out-of-plane deformation of the plate was large enough to distort the fringe patterns.

Several schemes for reducing the in and out-of-plane motion were tried, with limited success. These results will be reported on at a later date.

Thermal/Structural Analysis of a Flat Plate

A cyclic 2-D heat transfer analysis of the flat plate for the test conditions described for the laser tests was performed using MARC, a non-linear finite element thermal/structural analysis code. The plate was modelled with 192 finite elements. The heated plate was allowed to freely expand. The strains (stresses) were thermally induced as a result of the nonuniform temperature on the plate. Analyses were performed on the Lewis Cray XMP computer.

The predicted steady-state cool surface plate temperature for the maximum power condition (85 percent) and 221°C (430°F) cooling air to the plate is shown in Figure 16. Cooling air flows from right to left on the figure, with the coolest temperature in the lower right corner of the plate. The cooler temperatures along the right edge of the plate resulted from the cooling air being introduced to the plate through the manifold. The plate temperature increased as the cooling air heated up and was a maximum along the horizontal centerline and left of center of the plate. The centerline horizontal and vertical temperature profiles are in good agreement with the experimental data plotted in Figure 10.

A cyclic 2-D structural analysis of the flat plate was performed using MARC based on the measured and predicted thermal loads. The heat transfer finite element model was used for the structural analysis. Plane stress, four-node finite elements were used. There were 221 nodes with 442 degrees of freedom. The Walker model was used to predict the strains and stresses. It was implemented in MARC through a user subroutine, HYPELA. The predicted steady-state plate strains in the y-direction are shown in Figure 16 for the same conditions used for the thermal analysis. The maximum compressive strains are at the hot spot on the plate and at the center of the left edge of the plate. This is consistent with the plate distortion (see Fig. 8) that resulted from the thermal cycle imposed on the plate.

Annular Combustor Liner Test Facility
Structural Component Response Rig

Segments, or cylindrical sections of gas tur-
bine engine combustor liners were radiantly heated
in the Structural Component Response rig (shown
in Fig. 17) to induce thermal stresses and strains
in the test liners. Quartz lamps were used to
cyclically heat the test liners. This resulted
in axial and circumferential temperatures as well
as through-the-thickness temperature gradients
similar to those of in-service liners. A typical
engine mission cycle (take-off, cruise, landing,
and taxi) of three to four hours was simulated in
two- to three minutes. The simulated cyclic
temperatures and temperature gradients were felt
to be adequate to capture the time-independent
and time-dependent (creep/plasticity) interactions
resulting in deformation as well as the low-cycle
thermal fatigue phenomena of in-service liners.
The primary purpose of the rig was to generate
large quality TMD test data bases for prototypical
combustor liners.

The test program was a cooperative effort
with Pratt and Whitney Aircraft (PWA), a division
of United Technologies Research, East Hartford,
Connecticut. PWA supplied the test rig, which
included the quartz lamp heating system and
several test liners. The heating system was
designed and built by Research, Inc., Minneapolis,
Minnesota, under contract to PWA. Lewis provided
the test facility and had the responsibilities
from integrating the test rig into the test
facility up to and including conducting the tests
and acquiring the data. Lewis and PWA personnel
developed automated computer control strategies,
data acquisition systems, and methods for
efficient data reduction and analysis.

Description of Test Rig

The quartz lamp heating system consists of
sixteen reflector lamp banks, or zones, arranged
in a cylindrical array. Each zone contains seven
IR lamps mounted in parallel. The lamps are rated
at 6,000 watts, 480 volts. Total rated power is
672 kW, but because of lamp heating interactions
the maximum available power is approximately 580
kW.

Power provided to the test stand is three
phase, 480 volts. Four Silicon Controlled Recti-
fiers (SCR's) are used to distribute power to the
16 zones. Two SCR's control the power to twelve
zones, size zones each. The other two SCR's con-
trol the power to four zones, two zones each.

The same Dual Loop Programmable Controller
described for the Bench-Top Rig controls the power
signal to the SCR's. The set point control mode
is used for most tests to impose desired tempera-
ture histories at a point on the hot side of the
test liner. Similar to the Bench-Top rig, the
power histories programmed into the controller
were obtained from a set of parametric power

psig)
and 5.67 kg/sec (12.5 lb/sec). Of this total
flow, up to 3.40 kg/sec (7.5 lb/sec) can be
diverted to cooling the test liner. The liner
cooling air can be preheated with precise control
up to 316°C (600°F) by burning a controlled mix-
ture of air and natural gas in a combustor can.

The remaining cooling air flow is used to cool
the IR lamps and end seals, and six quartz window
viewports. The windows are cooled to minimize
distortion to the IR thermal images. The test
rig is designed for a maximum supply air pressure
of 0.34 MPa (50 psig). The nominal cooling air
pressure in the test section is 0.21 MPa (30
psig). All inlet/outflow flow conditions are
sensed and monitored and are available as visual
readouts or can be stored on the Lewis IBM 370
computer using the ESCORT II Data Acquisition
system.

Cooling water is required to cool the reflec-
tors, busbars, and viewports. A closed-loop
cooling system containing demineralized water,
which is cooled by process water in a heat
exchanger, cools the heating system. The view-
ports are cooled by process water. All inlet/
outlet water flow conditions are sensed and
monitored, and are available as visual readouts
or can be stored on the IBM 370 computer.

A more complex system of safety interlocks
than that described for the Bench-Top rig is pro-
vided to assure safe operation of the rig, to
protect personnel, and to avoid damage to the
test facility, rig and specimen.

Description of Test Liner

A photograph of the conventional test liner
is shown in Figure 18. The test liner, of sheet
metal seam welded louver construction, is a
nickel-base superalloy material, Hastelloy X.
The eight louvers are segments of an outer annulus
of a combustor liner. The test liner has an
inside diameter of approximately 50.8 cm (20
in.). Circumferential arrays of cooling holes
cool the louver lips. Louvers 4, 5, and 6 are
the active test louvers, that is, where the heat
flux to the test liner is considered to be rela-
tively flat. The IR lamps heat about 25.4 cm (10
in.) of the test liner.

Test Liner Temperature and
Displacement Measurements

Temperature data were obtained from Chromel/
Alumel thermocouples mounted on the cool and hot
surfaces of the test liner. A total of 106 ther-
mocouples were installed on the liner, 72 on the
cool surface and 34 on the hot surface. Clustered
sets of thermocouples on louvers 4 and 5 provided
detailed temperature measurements. The clustered
sets of thermocouples with a surface area of 7.6
x 10.2 cm (3 x 4 in.) were installed such that
the liner temperatures were measured directly
above one of the lamp zones. Limited axial and
circumferential temperature data were also
obtained at other critical locations on the liner.
In addition, an Infrared Thermovision system,
described previously, was used to obtain cool-
side temperature data. IR data were obtained by
the use of six viewports (quartz windows)
Fig. 17).

was used during the test to control the quantity
of data. The thermocouple data were recorded on
the IBM 370 or hard copy devices in the control
room. The acquisition system also provided for
easy access and plotting of the stored data.
Twenty different plots, including transient plots,
for any specified thermal cycle can be called up

for review and analysis of the data. The IR temperature data were recorded on a Video Cassette Recorder (VCR). The computer system coupled with the IR system described previously, provided for quick analysis of the data. Real time strip chart and molygraph devices were also used for data monitoring and recording.

Similar to the Bench-Top rig, the measured temperatures were not only used as thermal loads (inputs) to the structural analysis computer programs, but also as boundary conditions and for the determination of heat transfer coefficients. Heat transfer analyses were performed to determine liner temperatures. The predicted temperatures were used as thermal loads (inputs) to the structural analysis programs.

Measurement of test liner strain at the elevated temperatures (above 538°C (1000°F) is not possible with today's technology. However, advances in high temperature strain measurement technology should make it possible to measure strain at higher temperatures in the near future. As has been discussed, high temperature wire resistive strain gages, high temperature proximity (capacitive) transducers, and laser interferometric (specklegram) strain measurement systems have been or will soon be evaluated using the Flat Plate Bench-Top rig. Those systems which are shown to have potential will then be used on the Structural Component Response rig.

Since high-temperature strain measurements are not possible at this time, limited displacement measurements on the test liner were taken. They were, however, very time consuming since the liner had to be removed from the test rig to take the measurements. These measurements were taken periodically using a Cordax automated system. Radial measurements for louvers 3, 4, 5, 6, and 7 were taken at the lip and a point directly above the lip at 2.5 degree increments, for a total of 1,440 measurements. These measurements of liner distortions and lip closures can be compared to predicted displacements for verification of improved and newly developed constitutive models and other analytical tools.

Description of Thermal Cycle

A total thermal cycle time of 2.2 minutes was used to simulate an engine mission cycle consisting of climb (engine acceleration), cruise, descent (engine deceleration), and taxi flight conditions. It is broken up into four segments: a six-second ramp up from minimum to maximum power; a one-minute hold time at maximum power; a six-second ramp down from maximum to minimum power; and a one-minute hold time at minimum power. Two sets of cyclic test conditions were used.

The nominal cyclic test conditions consisted of a maximum power setting of 83 percent, a cooling air flow rate of 2.5 kg/sec (5.5 lb/sec) and the cooling air preheated to 316°C (600°F). These test conditions resulted in a maximum measured liner temperature on the hot surface of about 943°C (1730°F) and a cool surface measured temperature of about 382°C (750°F). The minimum power setting of 40 percent with the same flow and preheated cooling air conditions resulted in a maximum liner temperature of about 593°C (1100°F) and minimum temperature of about 316°C (600°F). These test conditions resulted in minimal distortion to the liner.

A second set of test conditions was used to accelerate the liner distortion and damage. In these tests the maximum percentage power was increased from 83 to 87 and the cooling air flow rate was reduced from 2.5 to 2.38 kg/sec (5.5 to 5.25 lb/sec) while all other test conditions were the same. These changes in test conditions resulted in increasing the maximum hot-side liner temperature to about 1010°C (1850°F) and a cool-side liner temperature of about 390°C (775°F). The delta hot-side temperature between the test conditions was about 56°C (100°F) and resulted in accelerating the liner distortion. The liner temperatures for the minimum power condition remained unchanged.

Temperature Measurements

Over 1300 thermal cycles have been accumulated on the test liner. About 41 percent of the cycles were run at the higher maximum power setting and lower liner cooling air flow. These conditions were set, as mentioned earlier, to accelerate distortion and damage to the liner. Liner surface temperatures from cycle-to-cycle and run-to-run were reproducible. The higher liner temperatures from run-to-run generally varied by +14.0°C (25°F). Shown in the following plots are stabilized cool surface temperatures obtained from the thermocouples for thermal cycle 1280, the more severe thermal cycle.

Shown in Figure 19 are the cool surface axial liner temperature variations at the maximum and minimum power levels of the thermal cycle. The thermocouples were located at the middle of each of the eight louver seam welds and were equally spaced at 3.5 cm (1-3/8 in.). The data points are not connected since there is considerable temperature variation between them. Note that the temperatures are relatively flat for louvers 4, 5, and 6.

Shown in figure 20 are the cool surface circumferential liner temperatures for the maximum and minimum power levels of the thermal cycle. Sixteen thermocouples are located at the middle of the louver 5 seam weld and are equally spaced such that they are aligned along the centerline of each of the sixteen lamp zones. These locations are approximately where the maximum temperatures occurred for each zone. The data points are not connected since there are temperature variations between them. Note that the temperatures are not uniform. The hottest cool-side liner temperature was 869°C (1597°F).

Temperatures from the clustered set of cool surface circumferential thermocouples (for a single lamp zone) are shown in figure 21 for the maximum and minimum power levels. The temperatures plotted were measured with thermocouples mounted at the seam weld of louver 5. The data show the temperatures to be scalloped. Note that the temperature difference is a representative measure of the temperature scalloping for this and other lamp zones and is about 222°C (400°F) for the maximum power condition. The temperature scalloping is representative of in-service liners where the scalloping results from the positioning of the fuel nozzles.

Detailed axial cool-surface temperatures for louvers 4 and 5 are shown in figure 22 for the maximum and minimum power levels of the thermal cycle. Thermocouples are spaced at variable increments down the centerline of a lamp zone. Here it becomes evident as to why data points for other axial plots of a temperature at a point on

each louver were not connected. For the maximum power condition, the temperature varies from 371°C (700°F) at the cool spot (near the cooling holes) to 816°C (1500°F) at the hot spot (close to the seam weld). For the minimum power condition, the temperature varies from 316°C (600°F) at the cool spot to 593°C (1100°F) at the hot spot.

Having detailed temperature information from thermocouples at relatively closely spaced locations is still no guarantee that an accurate temperature variation can be plotted. This became evident when data from the IR Thermovision system scans were examined. Shown in figure 23 is the complex temperature pattern on the cool side. Each shade of grey represents a different temperature range. This shows why the temperature data points were not connected. There is almost a step change in temperature from one louver to the next which would go unnoticed if only thermocouple data were used.

Centerline axial temperatures from the clustered set of thermocouples on the hot surface of the test liner, along the same centerline of a lamp zone as the cool surface axial temperatures (see Fig. 22) are plotted in Figure 24. Here again, temperatures are plotted for stabilized maximum and minimum power conditions for louvers 4 and 5. Note the temperature discontinuity at the louver lip, that is, where louver 4 ends and louver 5 begins at a point downstream of the cooling holes (knuckle). These two points lie on the same radial line. Note also that the hot spot lies very near the seam weld. However, the hot surface hot spot of a conventional in-service liner is generally at the louver lip.

Shown in figure 25 are hot surface circumferential temperatures at the same points (seam weld) as the cool surface circumferential temperatures plotted in figure 21. Temperatures were plotted for stabilized maximum and minimum power conditions for louvers 4 and 5. Here again, there is a temperature variation over the width of the lamp zone. As was the case for the cool surface, the circumferential temperatures are obviously nonuniform, that is, the temperatures are scalloped from zone to zone.

Hot surface transient temperatures are plotted in figure 26 at three potentially critical failure locations on the liner: (1) at the louver lip, (2) at the seam weld, and (3) at a point near the seam weld. Note that it takes about 25 seconds for the temperatures to stabilize both on the heat-up and cool-down phases. Recall that the power to the lamps is ramped up and down in six seconds for each thermal cycle, so there is about a 15-second temperature lag between maximum power and a stabilized temperature on the liner.

What has been presented here in terms of liner temperature plots is only a brief summary of the large quality temperature data base available. Much more data are available, both thermocouple and infrared, and they are being reduced and analyzed. The reduced data will be used for both numerical heat transfer and structural analyses.

Displacement Measurements

In addition to the liner measured temperatures obtained, some liner displacement measurements were also taken. Radial displacement measurements were taken before the test began and after thermal cycles 300, 742, and 1280. Radial measurements in the circumferential direction were taken at the lips of louvers 3, 4, 5, 6, and 7 and at a radial point directly above the lip (the next louver). The difference between the radial measurements is the lip closure. Plotted in figure 27 are the relative radial displacements for louver lip 5 and louver 6 for the undeformed liner and the deformed liner at the end of thermal cycle 742. With these measurements, the distortion of the liner at a radial location can be monitored as a function of the number of thermal cycles. Note the liner distortion is consistent with the temperature scalloping, that is, symmetric with the lamp zones, and results from the uneven circumferential heating, as indicated in the circumferential temperature plots.

Photographs of the cool and hot surfaces of the test liner were taken periodically to document the liner distortion as well as the condition of liner. Shown in figure 28 is a photograph of the hot surface of the test liner at the end of thermal cycle 1280. Not only is the liner distortion documented, but qualitative measurements of the distortion can also be obtained from the photographs. The liner distortion shown does simulate the types of distortion observed in in-service liners. Tests on the liner will continue until either the liner distorts badly or liner cracking occurs.

Test Liner Heat Transfer Analysis

A 2-D axisymmetric heat transfer analysis of the test liner was performed using MARC. Louver 5 was modelled with ten axisymmetric ring finite elements. The analysis discussed here was performed for the more severe thermal cycle test conditions described previously.

The temperature data obtained were used in the heat transfer analysis as boundary conditions (thermal loads) and to determine the heat transfer coefficients on the cool and hot surfaces of the liner. An iterative heat transfer analysis of the test liner was performed to determine the heat transfer coefficients. Shown in figure 29 are the 2-D heat transfer coefficients determined for louver 5 along the centerline of one of the lamp zones. The much higher heat transfer coefficients near the knuckle simulate the cooling holes.

Shown in Figure 30 is a predicted isothermal plot for the stabilized maximum power (cruise), or temperature, conditions. The hot spot on the liner is at or very near the seam weld. In this case, on the hot surface, the predicted temperatures vary from about 593°C (1100°F) to 954°C (1750°F). There is good agreement between predicted and measured temperatures on both the hot and cool surfaces of the liner. The measured temperature at the louver lip is about 899°C (1650°F). Temperatures (predicted and measured) at the louver lip of the test liner are generally lower (by about 55°C (100°F)) than those of in-service liners. Note also that the through-the-thickness (radial) delta temperatures are about 72°, 28°, and 22°C (130°, 50°, 40°F) at the seam weld, lip and knuckle, respectively. These delta temperatures simulate those of in-service liners. Only a 2-D heat transfer analysis has been performed to date, but it is evident from the temperature plots presented previously that a 3-D heat transfer analysis must be performed in order to accurately predict the multiaxial states of stress and strain in the liner.

Test Liner Structural Analysis

The measured and predicted temperatures were used as input (thermal loads) to the structural analysis program. The MARC program was used to predict the nonlinear structural response of the same 2-D axisymmetric finite element model of louver 5 that was used in the heat transfer analysis. Ten axisymmetric ring elements with 51 nodes were used to describe the louver geometry. This resulted in 102 degrees of freedom. Appropriate boundary conditions (slopes and displacements) were assumed. The unified Walker constitutive model was used in the structural analysis to predict liner strain-stress responses. The model was incorporated in the MARC through a user subroutine HYPELA.

Shown in Figures 31 and 32 are 2-D contour plots of the hoop strain and stress predictions using the Walker model for louver 5 at the minimum and maximum power (simulated taxi and cruise) conditions for thermal cycle 1280. Maximum hoop strains for both the simulated taxi and cruise conditions occur at the seam weld of the liner, or very near the hot spot on the liner, with values of approximately 0.26 and 0.73 percent. On the other hand, maximum hoop stresses for both simulated conditions occur at the seam weld and knuckle, with values of approximately 310 MPa (45 ksi) and 393 MPa (57 ksi).

Not only are accurate predictions of maximum stresses and strains important in determining the durability of liners, but equally important are accurate predictions of the transient stresses and strains. Figure 33 shows the predicted temperature history for three potentially critical liner failure locations at the lip, knuckle, and seam weld of louver 5. Shown in Figure 34 (a, b, c) are plots of the predicted hoop strain histories and stresses for the three liner locations. Note in these plots the rather large differences in strains, the shapes of the curves and whether the strains are in-phase or out-of-phase with the temperatures depending on the location. Combined with temperature histories the strain histories should guide the test conditions chosen for development and validation of the models. This was the reason for the uniaxial nonisothermal temperature range chosen earlier.

Figure 35 shows the stress-strain response (hysteresis loops) predictions for the three liner locations. Here again, there are large differences in the cyclic responses depending on the location. This results from the different temperature history at each location. Only 2-D analyses were conducted, but as is evident from the temperature plots, 3-D analyses are required for accurate determination of component durability.

There are no simple or well-established procedures for evaluating and validating the 3-D steady-state and transient stress-strain response predictions in nonlinear structural analysis of complex gas turbine engine hot section components. To date, the evaluation and validation of the unified models have been based primarily on isothermal uniaxial tests and a limited number of nonisothermal proportional and nonproportional loadings (thermomechanical deformation) uniaxial tests. Further, there is the question as to whether or not the material constant determined from isothermal uniaxial tests for the unified models are applicable for accurate prediction of

even nonisothermal uniaxial cyclic responses, let alone isothermal and TMD biaxial predictions. In addition, the high-temperature isothermal and nonisothermal deformation testing of materials has been limited for several reasons. Some of the difficulties are: limited testing capabilities for precise loading (stress, strains, displacements, or loads and temperatures) control; heaters/furnaces to produce the desired steady state and cyclic temperatures, temperature rates, and temperature gradients; advanced instrumentation (contact, noncontact, optical) to measure local temperatures and strains and/or displacements; software to control the deformation experiments, acquire the data, reduce it and analyze it; test machines to reproduce principal biaxial stress/strain space of in-service components (probably requires an internal and/or external pressure fixture); large test machines capable of reproducing a 3D stress/ strain space of in-service liners and other hot section components; and even such "minor" things as designing high temperature grips for specimens as well as the specimen design.

Concluding Remarks

Evaluation and validation studies of four unified constitutive materials models (Miller, KSR, Bodner, and Walker) for structural analysis of gas turbine engine hot section components were conducted. But the limited experimental data (uniaxial generated cyclic isothermal and nonisothermal) made it difficult to make definitive judgments as to which model constitutes the best approach for the hot section component application. Qualitatively, the uniaxial model prediction of the nonlinear material behavior of Hastelloy-X compared, in a general sense, reasonably well with the experimental data. But quantitatively, to accurately predict the shapes and levels of the cyclic stress-strain responses will require further refinements to the models. It was also evident that as the complexity of deformation testing, and modeling, increased, that is, in going from monotonic to cyclic to isothermal to nonisothermal, the agreement between prediction and experiment was progressively worse. Overall comparisons between the uniaxial predictions and experiments showed that the Bodner and Walker models were better able to predict the nonlinear structural responses. A new high-temperature structural components response test facility has been constructed at NASA Lewis for the purpose of testing complex geometry specimens under simulated engine mission cycle conditions. Two rigs were used for the thermomechanical deformation and durability testing of flat plate specimens and large diameter sections of combustor liners. Both rigs used quartz lamps to heat the specimens. The research rigs were shown to be viable, flexible, and reliable and produced large quality data bases for structural analyses and evaluation of newly developed and improved analytical tools.

The test data obtained consisted of large amounts of temperature and displacement measurements as well as photographs of the distortion as the number of thermal cycles were accumulated on the test specimens. The test rigs produced controlled specimen cyclic temperatures typical of in-service combustor liners. For example, the temperatures on the combustor test liner ranged from a minimum of about 371°C (700°F) near the

cooling holes to a maximum of about 982°C (1800°F) on the hot surface of the liner. These test results, particularly for the combustor test liner, are possible benchmarks for future evaluation and validation of structural analysis and life prediction tools. These temperatures resulted in minimal distortions to the test liner. To accelerate distortion to the test liner, the liner maximum temperature was increased about 56°C (100°F) by increasing the maximum power level to the quartz lamps and reducing the cooling air flow. Significant liner distortion resulted from the higher liner temperatures. The combustor liner test simulated the low cycle fatigue, creep, and damage mechanisms of in-service liners and the liner distortion was similar to that of in-service liners.

Advanced instrumentation for measuring temperature and strain was evaluated on both test rigs. An Infrared Thermovision system for measuring temperature showed two distinct advantages over thermocouples. First was the ability to obtain cyclic temperature maps of the cool side of the test specimens. Second was the ability to measure specimen temperatures where large temperature gradients occurred over small distances. The potential for using a noncontact device to measure local strain, the Laser Specklegram system, was also shown on a flat plate specimen.

Combined two-dimensional heat transfer and structural analysis of a flat plate specimen and combustor test liner were conducted using a general purpose nonlinear finite element code. For both test specimens, the steady state and cyclic temperature predictions were in good agreement with the measured temperatures. For the structural analysis of the specimens, the four unified models were implemented in the general purpose code. Based on the uniaxial experimental and predictions, the Walker model was used to predict the thermally induced multiaxial stresses and strains. The structural response predictions of the test liner that resulted from the assumed complex cyclic thermomechanical load history varied greatly depending on the liner location analyzed. These results illustrated the need for having nonlinear constitutive models that accurately predict the coupled time-independent and time-dependent multiaxial states of stress and strain over a wide range of variables. Some of these variables are: temperature amplitudes, ranges and rates; strain or stress amplitudes, ranges and rates; multiaxial proportional and nonproportional mechanical loads; isothermal and nonisothermal loads; and complex cyclic thermo-mechanical load histories, including both in-phase and out-of-phase. It is these predicted results of complex geometry specimens that should serve as a guide to determine what tests should be included in the uniaxial and multiaxial test matrices for the evaluation and validation of the analytical tools developed. This is essential since in testing complex structural components it is impractical, if not impossible, to measure stresses. Having accurate predictions of stresses and strains for these components is essential for accurate prediction of component durability. Also, as evident from the temperature and displacement measurements obtained and the distortion of the test specimens that two-dimensional thermal and structural analyses are not adequate to accurately predict the multiaxial stress-strain states in turbine engine hot section components. Thus, three-dimensional analyses and tests are required for the durability assessments of complex geometry components.

NASA's response to advancing the technology, both analytically and experimentally, to improve the nonlinear structural analysis capabilities of gas turbine engines, which is formidable, involves a team of researchers working in key areas from other government agencies, industry, and academia, each with its particular technical expertise and each complementing the other. The critical elements for the technological advances to occur are: improvements in nonlinear constitutive model development and validation; nonlinear analytical methodologies development and validation; experimentation to support model and analytical methodologies development and validation; and computational methods development. NASA Lewis has an Integrated Structural Mechanics program in which each of the critical elements is being addressed through combined contract, grant, and in-house efforts. From the results presented here and elsewhere, it is evident that a multifaceted, multidisciplinary effort has evolved and has already resulted in many significant advances in high-temperature nonlinear structural analysis capabilities. Further, with the contract, grants, and in-house activities currently underway and planned, as well as new and unique experimental facilities completed, nearing completion and planned at NASA Lewis and elsewhere, there will be an increasing number of significant advances in nonlinear structural analysis capabilities in the very near future. These new and improved analysis capabilities can be applied not only to the aerospace industry but also to other industry.

References

1. McKnight, R. L., Laflen, J. H., and Spamer, G.T.: Turbine Blade Tip Durability Analysis. General Electric Co., Cincinnati, OH, NASA CR-165268, Feb. 1981.

2. Moreno, V.: Combustor Liner Durability Analysis. Pratt a Whitney Aircraft Group, E. Hartford, CT., NASA CR-165250, Feb. 1981.

3. Walker, K. P.: Research and Development Program for Nonlinear Structural Modeling with Advanced Time-Temperature Dependent Constitutive Relationships. United Technologies Research Center, E. Hartford, CT., NASA CR-165533, Nov. 1981.

4. Cassenti, B. N.: Research and Development Program for the Development of Advanced Time-Temperature Dependent Constitutive Relationships. United Technologies Research Center, E. Hartford, CT, NASA CR-168191, July 1983.

5. Miller, A. K.: An Inelastic Constitutive Model for Monotonic Cyclic and Creep Deformation: Part I – Equations Development and Analytical Procedures, and Part II – Application to Type 304 Stainless Steel. ASME J. Eng. Mat. and Tech., Vol. 98, pp. 97-113, 1976.

6. Krieg, R. D., Swearengen, J. C., and Rhode, R. W.: A Physically Based Internal Variable Model for Rate-Dependent Plasticity in Inelastic Behavior of Pressure Vessel and Piping Components. PVP-PB-028 (ASME), pp. 15-28, 1978.

7. Bodner, S. R. and Partom, Y.: Constitutive Equations for Elastic-Viscoplastic Strain-Hardening Materials. Journal of Applied Mechanics, Vol. 42, pp. 385-389, June 1975.

8. Lindholm, U. S., Chan, K. S., Bodner, S. R., Weber, R. M., Walker, K. P., and Cassenti, B. N.: Constitutive Modeling for Isotropic Materials (HOST). Southwest Research Institute, San Antonio, TX, NASA CR-174718, May 1984.

9. Hirschberg, M.: A Low Cycle Fatigue Testing Facility. Manual on Low Cycle Fatigue Testing, ASTM STP 465, American Society for Testing and Materials, p. 67, 1969.

10. Chang, T. Y. and Thompson, R. L.: A Computer Program for Predicting Nonlinear Uniaxial Material Responses Using Viscoplastic Models. NASA TM 83675, July 1984.

11. Robinson, D. N. and Bartolotta, P. A.: Viscoplastic Constitutive Relationships with Dependence on Thermomechanical History. NASA CR-174836, March 1985.

12. Stetson, K. A.: The Use of Heterodyne Speckle Photogrammetry to Measure High-Temperature Strain Distributions. Holographic Data Nondestructive Testing, D. Vukicevic, Ed., Proc. SPIE 370, 1983.
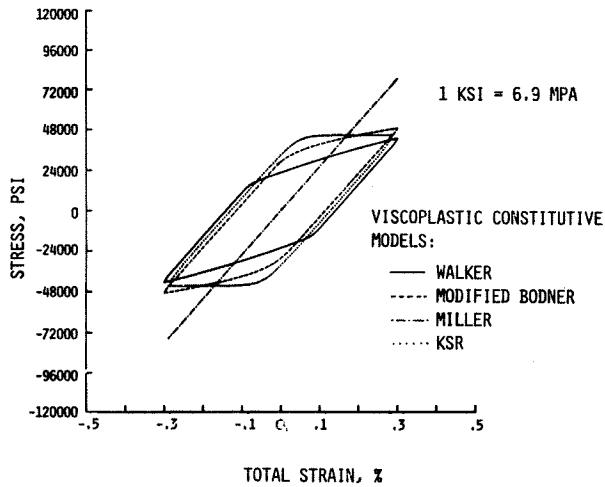
FIGURE 1 - COMPARISON OF UNIAXIAL ISOTHERMAL UNIFIED MODEL
PREDICTIONS FOR HASTELLOY-X AT 427 °C (800 °F).
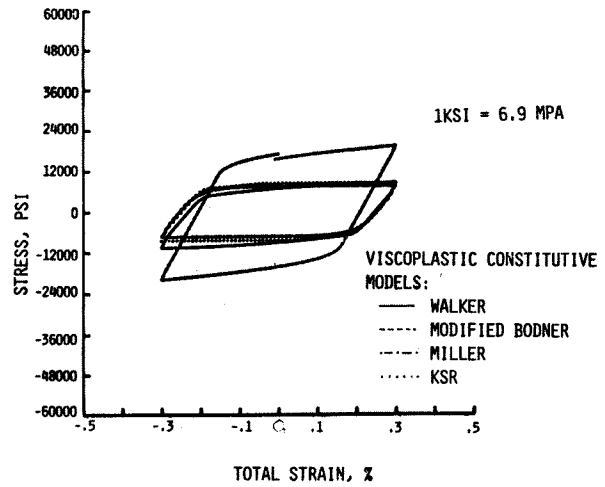
FIGURE 4 - COMPARISON OF UNIAXIAL ISOTHERMAL UNIFIED MODEL
PREDICTIONS FOR HASTELLOY-X AT 982 °C (1800 °F).
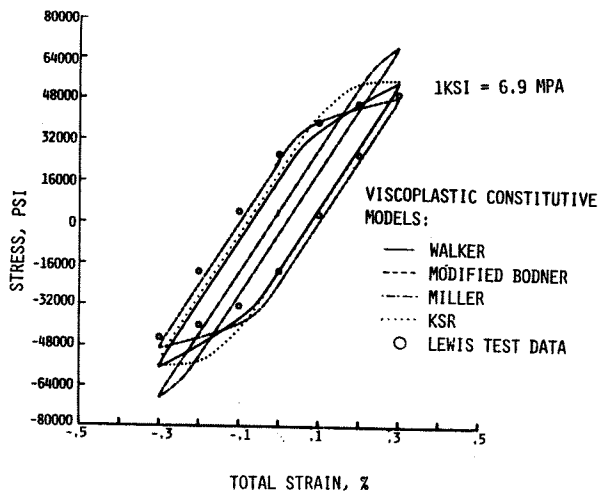
FIGURE 2 - COMPARISON OF UNIAXIAL ISOTHERMAL EXPERIMENTAL DATA
AND UNIFIED MODEL PREDICTIONS FOR HASTELLOY-X AT
593 °C (1100 °F).
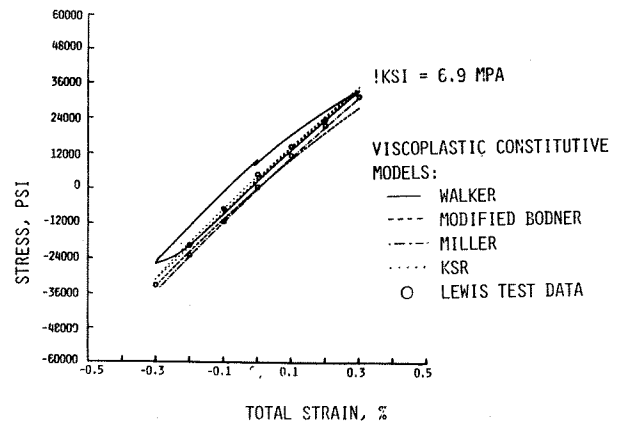
FIGURE 5 - COMPARISON OF IN-PHASE UNIAXIAL THERMOMECHANICAL
EXPERIMENTAL DATA AND UNIFIED MODEL PREDICTIONS FOR
HASTELLOY-X FOR TEMPERATURE RANGE OF 400-600 °C
(752-1112 °F).
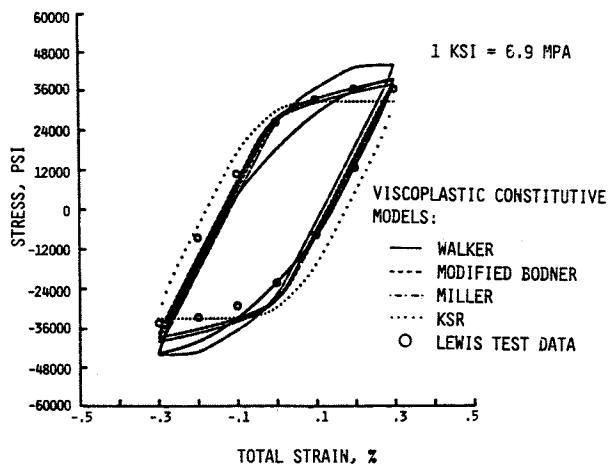
FIGURE 3 - COMPARISON OF UNIAXIAL ISOTHERMAL EXPERIMENTAL
DATA AND UNIFIED MODEL PREDICTIONS FOR
HASTELLOY-X AT 760 °C (1400 °F)
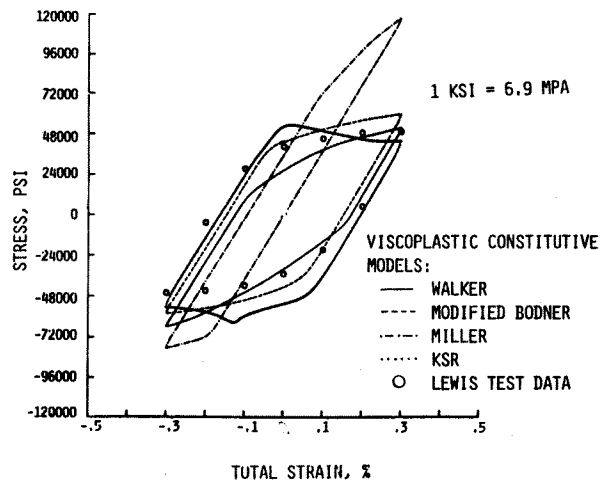
FIGURE 6 - COMPARISON OF OUT OF PHASE UNIAXIAL THERMOMECHANICAL
EXPERIMENTAL DATA AND UNIFIED MODEL PREDICTIONS FOR
HASTELLOY X FOR TEMPERATURE RANGE OF 400-600 °c
(752-1112 °F)

1505n
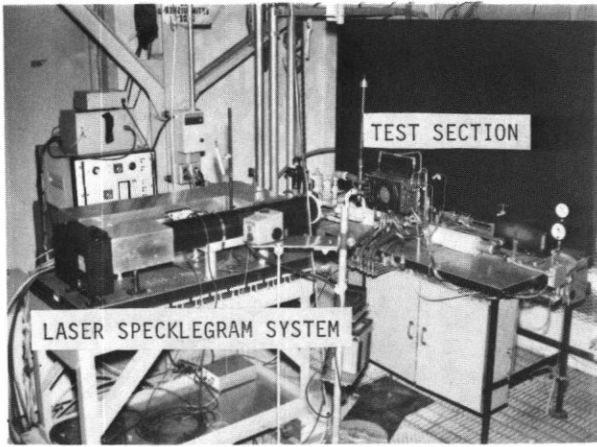
FIGURE 7 - FLAT PLATE BENCH-TOP RIG.
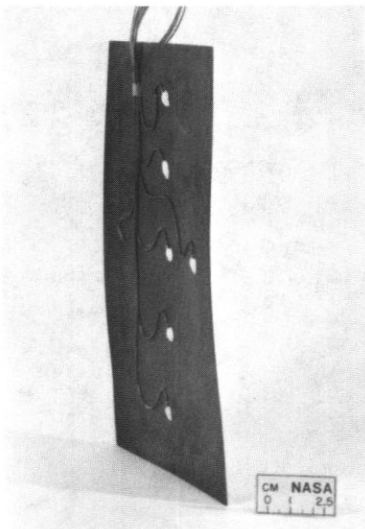
FIGURE 8 - FLAT PLATE HASTELLOY-X TEST SPECIMEN.
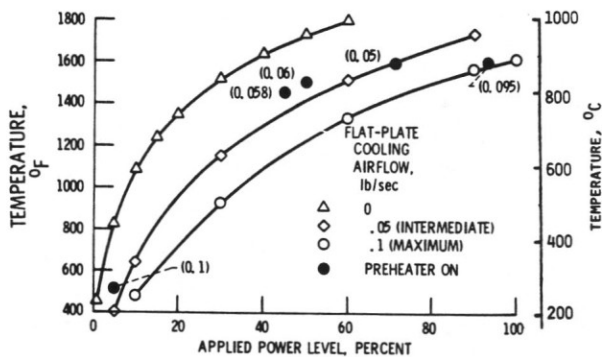
FIGURE 9 - MAXIMUM STEADY-STATE COOLSIDE TEMPERATURES ON HASTELLOY-X FLAT PLATE.
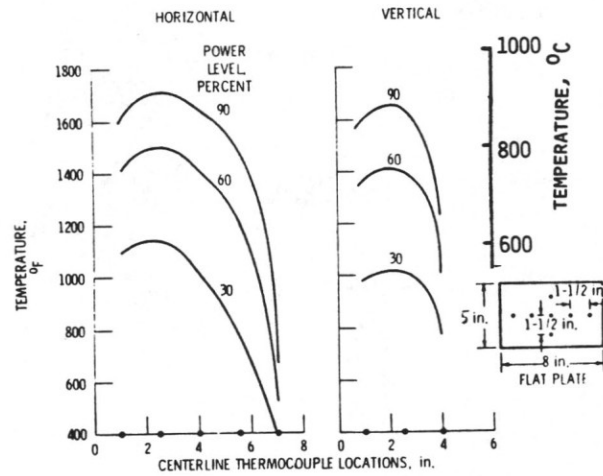
FIGURE 10 - STEADY-STATE COOLSIDE TEMPERATURES ON HASTELLOY-X FLAT PLATE FOR INTERMEDIATE COOLING AIR FLOW OF 0.5 LB/SEC.
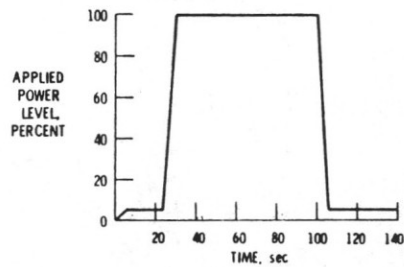
FIGURE 11 - APPLIED POWER HISTORY FOR REPRESENTATIVE THERMAL CYCLE IMPOSED ON HASTELLOY-X FLAT PLATE.
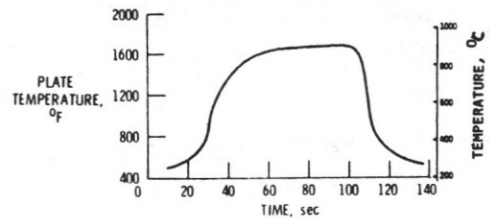
FIGURE 12 - TRANSIENT MAXIMUM COOLSIDE TEMPERATURE ON HASTELLOY-X FLAT PLATE.
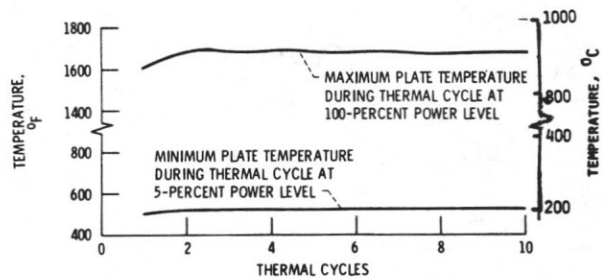
FIGURE 13 - THERMAL CYCLE VARIATION OF COOL-SIDE TEMPERATURES ON HASTELLOY-X FLAT PLATE.

x strain   shear   y strain
−382 μ   −255 μ   −1622 μ

THERMOCOUPLE
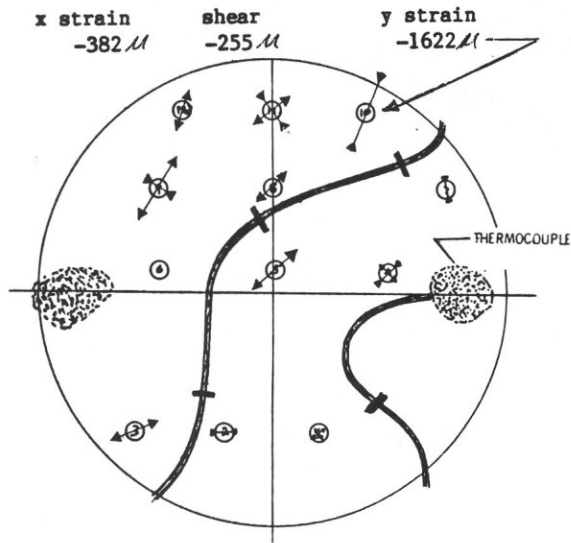
FIGURE 14 – PRINCIPAL STRAIN VECTORS OF
THERMALLY LOADED FLAT PLATE
HASTELLOY-X TEST SPECIMEN
OBTAINED FROM A LASER SPECKLE-
GRAM SYSTEM.

FIGURE 17 – STRUCTURAL COMPONENT RESPONSE RIG.

TEMP.,
DEG. F

1615.
1562.
1509.
1456.
1403.
1350.
1297.
1244.
1192.
1139.
1086.
1033.
980.
927.
874.
821.

FIGURE 15 – PREDICTED PLATE TEMPERATURE
AT MAXIMUM POWER.

LOUVERS

4
5
6
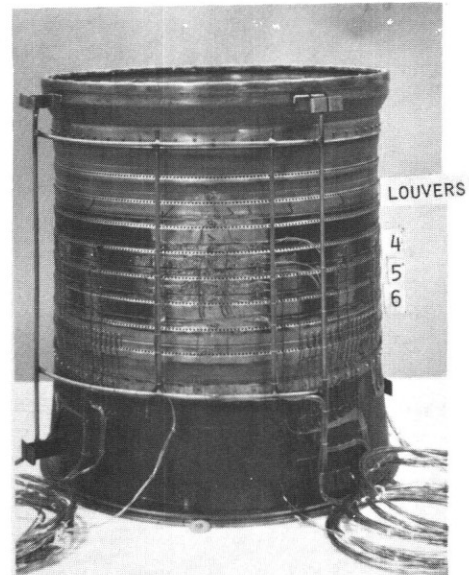
FIGURE 18 – CONVENTIONAL SHEET METAL LOUVER
LINER TESTED IN THE STRUCTURAL
COMPONENT RESPONSE RIG.

STRAIN
IN./IN.

.000136
.000113
.0000901   C
.0000672   D
.0000443
.0000214   F
−.00000144   G
−.0000243
−.0000472
−.0000701
−.0000930
−.000116
−.000139
−.000162
−.000185

STRAIN IN Y-DIRECTION (180 SECONDS)

FIGURE 16 – PREDICTED PLATE STRAIN AT
MAXIMUM POWER.

LOUVERS 4 AND 5

TEMPERATURE, $^{\circ}F$

TEMPERATURE, $^{\circ}C$

X   MAXIMUM TEMPERTURE
•   MINIMUM TEMPERATURE

AXIAL DISTANCE ALONG COMBUSTOR, IN.
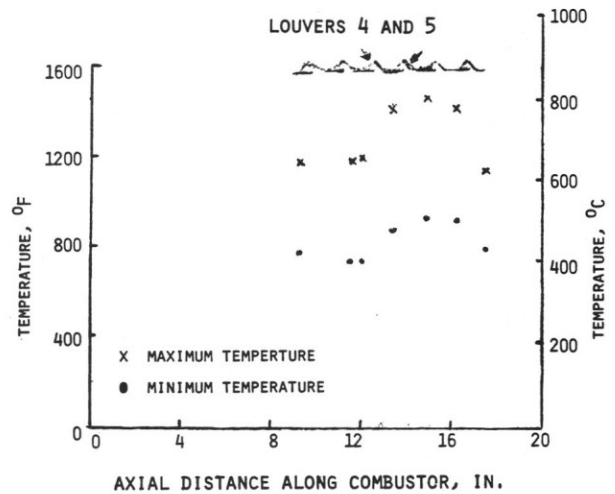
FIGURE 19 – COOL SURFACE AXIAL TEMPERATURES ON
COMBUSTOR LINER
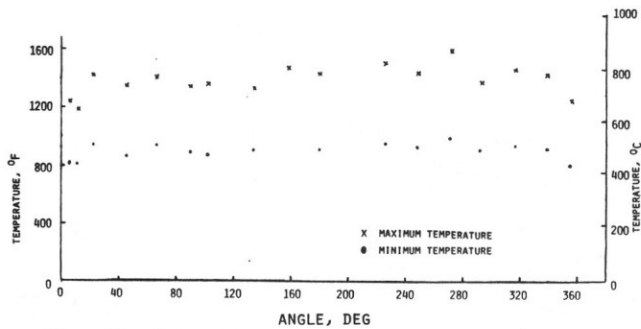
FIGURE 20 - COOL SURFACE CIRCUMFERENTIAL LINER TEMPERATURES
AT THE SEAM WELD OF LOUVER 5.
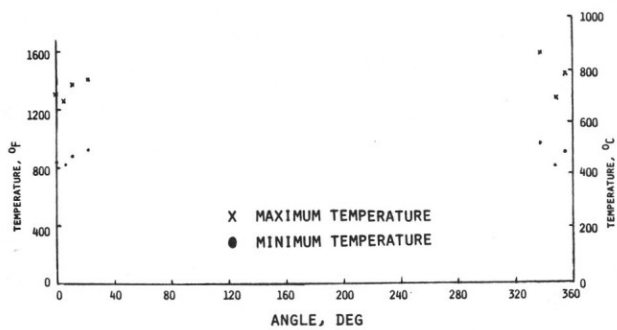
FIGURE 21 - COOL SURFACE CIRCUMFERENTIAL LINER TEMPERATURES
AT THE SEAM WELD OF LOUVER 5.
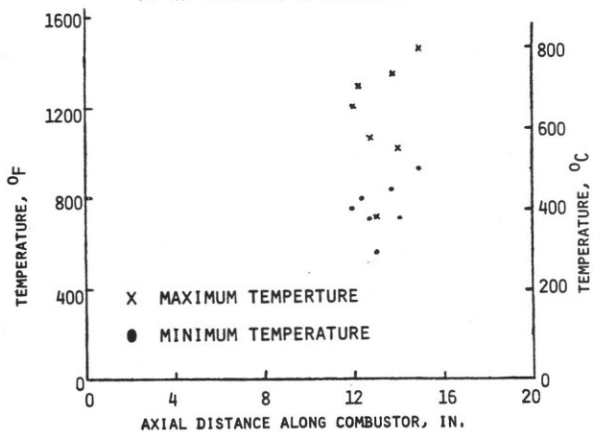
FIGURE 22 - COOL SURFACE AXIAL LINER TEMPERATURES
ON LOUVERS 4 AND 5.
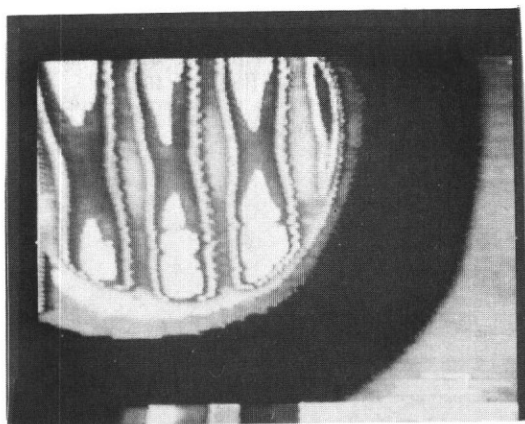
FIGURE 23 - THERMOVISION IR PICTURE OF LOUVERS 4, 5, AND 6
SHOWING COMPLEX HEAT PATTERN. EACH GREY SHADE
REPRESENTS A DIFFERENT TEMPERATURE RANGE.
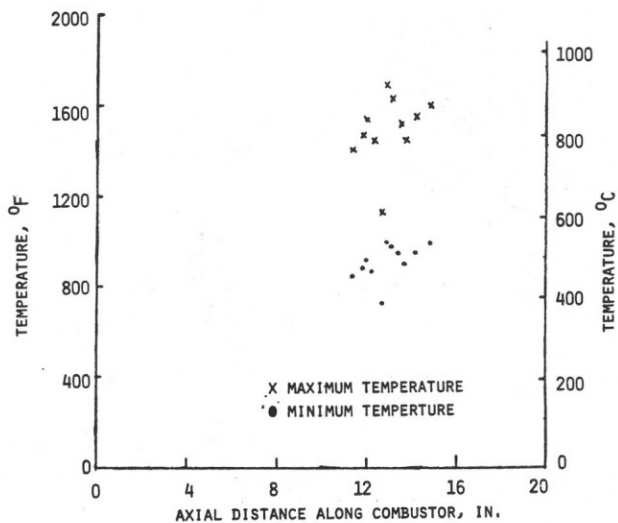
FIGURE 24 - HOT SURFACE AXIAL LINER TEMPERATURES
ON LOUVERS 4 AND 5.
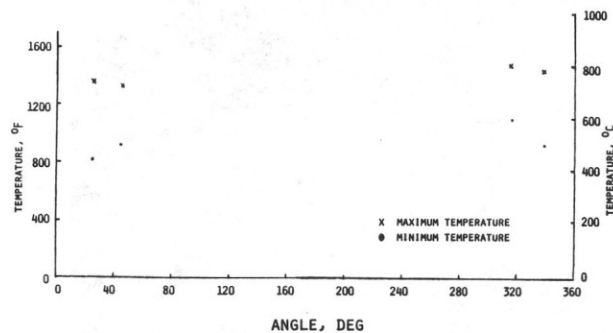
FIGURE 25 - HOT SURFACE CIRCUMFERENTIAL LINER TEMPERATURES
AT THE SEAM WELD OF LOUVER 5.
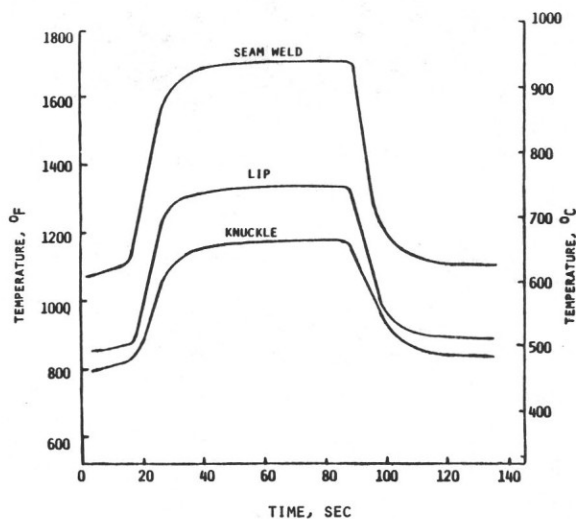
FIGURE 26 - CYCLIC HOT SURFACE LINER TEMPERATURES AT
THREE LOCATIONS ON LOUVER 5.
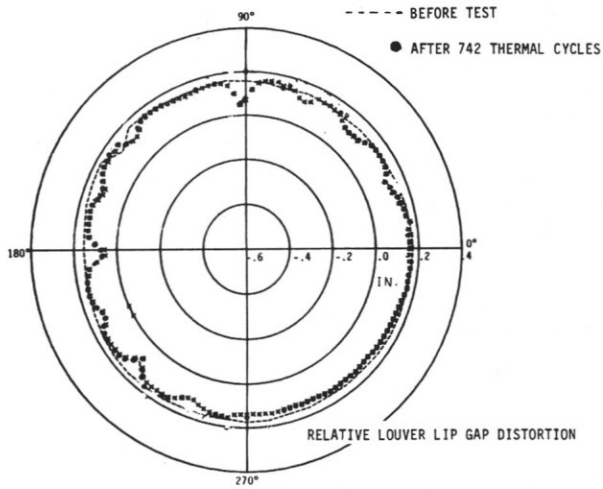
FIGURE 27 - COMPARISON OF UNDEFORMED AND
DEFORMED LINER RADIAL DISTORTION
OF LOUVERS 5 AND 6.
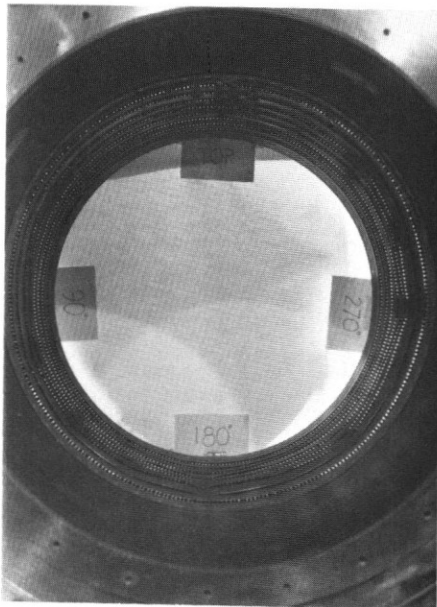
FIGURE 28 -- HOT SURFACE LINER DISTORTION AFTER
1280 THERMAL CYCLES.

IN Btu/ft²-hr - °F
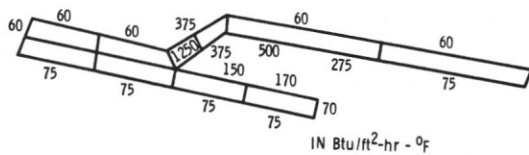
FIGURE 29- THERMAL FILM COEFFICIENTS FOR LOUVER 5.
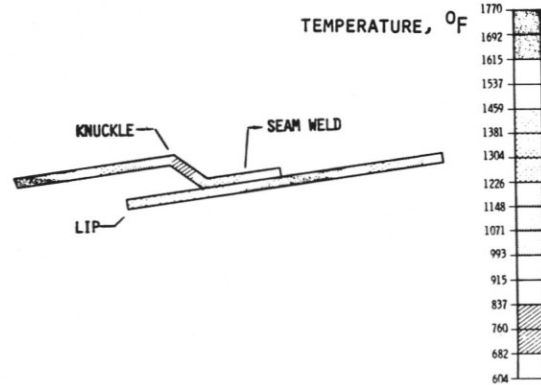
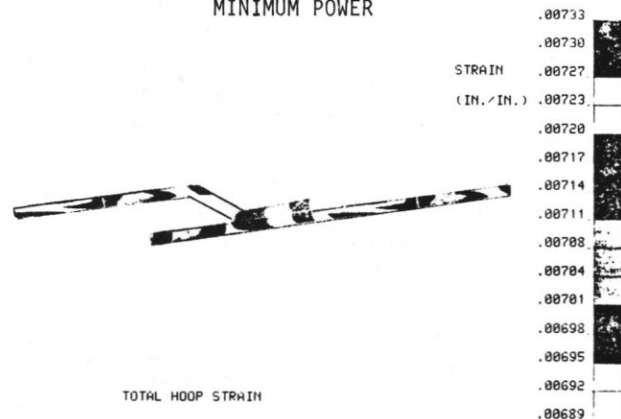FIGURE 30 - PREDICTED TEMPERATURES FOR
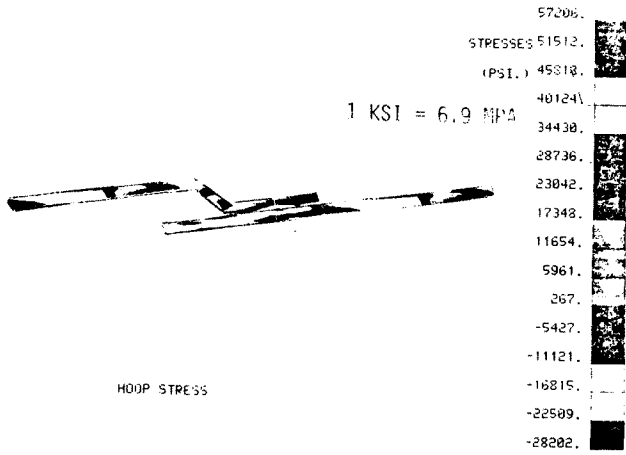LOUVER 5 AT MAXIMUM POWER.

1 KSI = 6.9 MPA
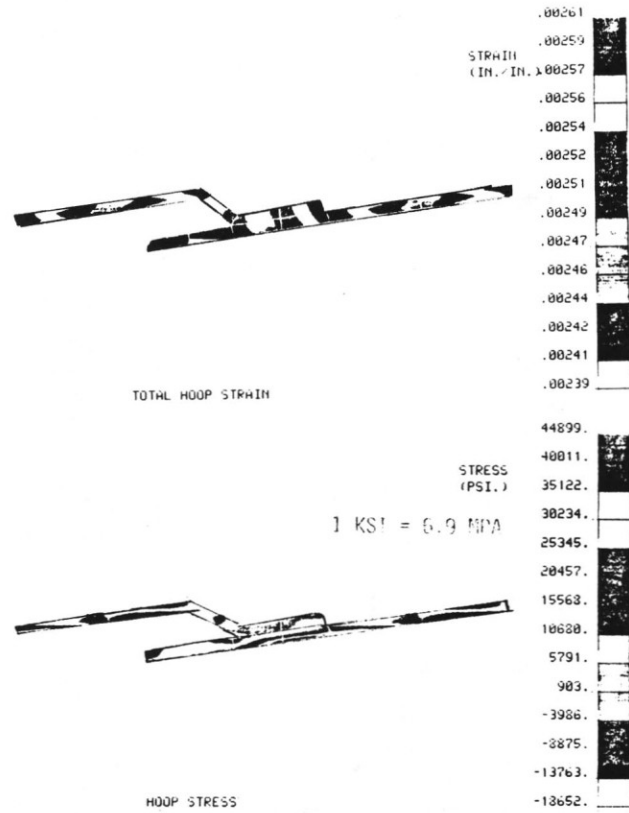
FIGURE 31 - HOOP STRAIN AND STRESS PREDIC-
TIONS USING THE WALKER
UNIFIED MODEL   FOR LOUVER 5 AT
MINIMUM POWER

STRESSES 57206.
(PSI.) 51512.
45818.
1 KSI = 6.9 MPA   40124
34430.
28736.
23042.
17348.
11654.
5961.
267.
-5427.
HOOP STRESS   -11121.
-16815.
-22509.
-28202.

FIGURE 32 - HOOP STRAIN AND STRESS PREDIC-
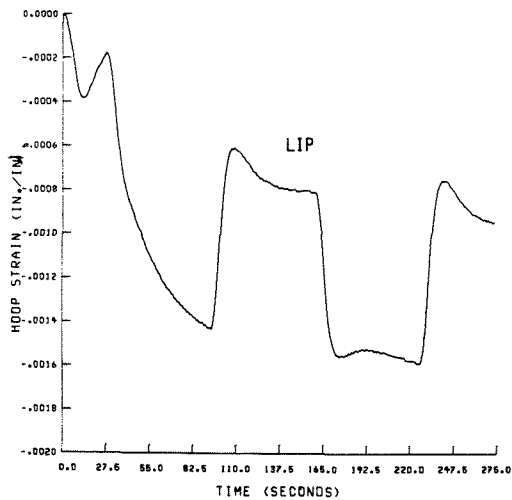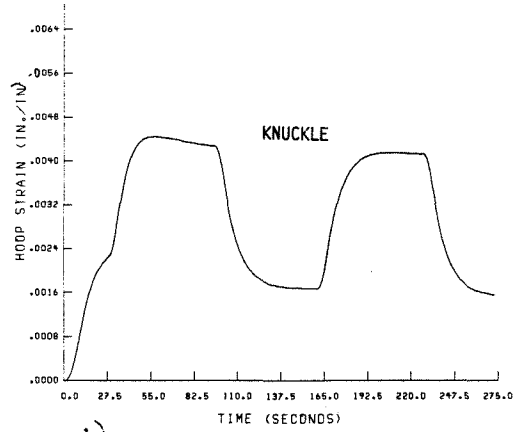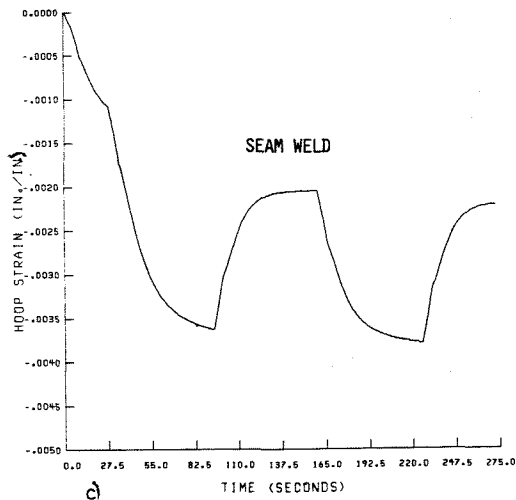TIONS USING THE WALKER
UNIFIED MODEL FOR LOUVER 5
AT MAXIMUM POWER.
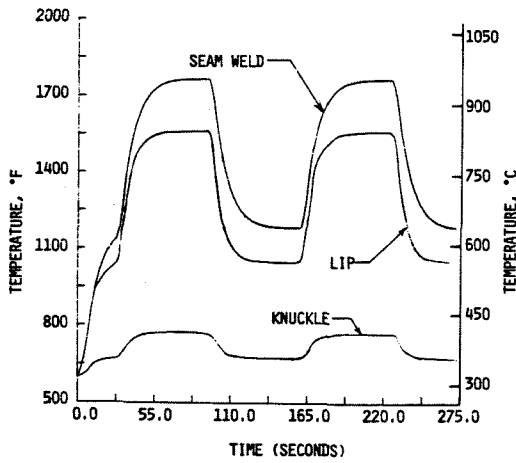
FIGURE 33 - REPRESENTATIVE 2-D COMBUSTOR LINER TEMPERATURE
HISTORIES AT THE LIP, KNUCKLE, AND SEAM WELD
OF LOUVER 5.

FIGURE 34 - REPRESENTATIVE 2-D COMBUSTOR
LINER HOOP STRAIN HISTORY
PREDICTIONS AT THE LIP, KNUCKLE
AND SEAM WELD OF LOUVER 5 USING
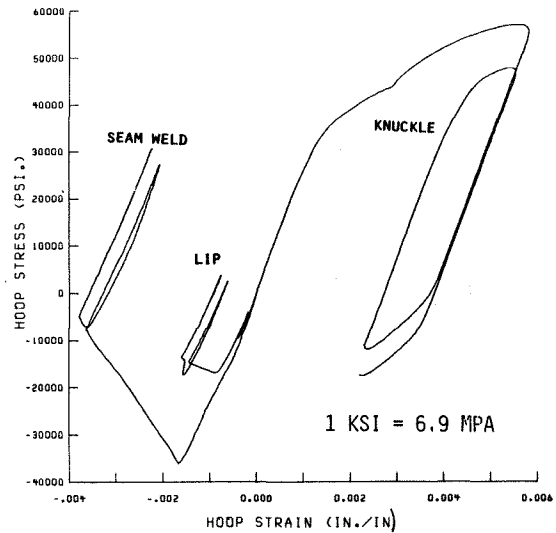THE WALKER MODEL.

1 KSI = 6.9 MPA

FIGURE 35 - REPRESENTATIVE 2-D COMBUSTOR
LINER HYSTERESIS LOOP PREDICTIONS
AT THE LIP, KNUCKLE AND SEAM WELD
OF LOUVER 5 USING THE WALKER
MODEL.

1505s